Metasurface-Based Dual Polarized MIMO Antenna for 5G Smartphones Using CMA

KAMEL S. SULTAN[1,2,3], **(Student Member, IEEE), HAYTHEM H. ABDULLAH**[1],
ESMAT A. ABDALLAH[1], **(Member, IEEE), AND**
HADIA S. EL-HENNAWY[2], **(Member, IEEE)**

[1]Electronics Research Institute, Giza 12622, Egypt
[2]Electronics and Communication Department, Faculty of Engineering, Ain Shams University, Cairo 31733, Egypt
[3]School of ITEE, The University of Queensland, Brisbane, QLD 4072, Australia

Corresponding author: Kamel S. Sultan (k.sultan@uq.edu.au; kamelsultan@eri.sci.eg)

ABSTRACT This paper exhibits a low profile dual-polarized MIMO antenna with high isolation to meet the requirements of 5G smartphones. The integration between a vertically polarized slot and a horizontally polarized slot is investigated and applied for 28 GHz dual-polarized smartphone antenna. The antenna is combined with metasurface (MTS) to achieve high gain and more directivity. In order to design the metasurface, the characteristic mode analysis is used to investigate the performance of MTS at 28 GHz. The proposed antenna achieves high isolation coefficients better than 40 dB and cross polarization lower than -40 dB from simulated and measured results. The isolation between elements is achieved without any additional decoupling techniques. The proposed MTS slot antenna operates with 4 GHz bandwidth (26-30 GHz) with a realized gain of 11 dBi and efficiency of 90%. Four antennas (with eight ports) are positioned orthogonally at the corners of the mobile PCB to serve MIMO for 5G applications. The effect of MIMO antenna on the human is taken into consideration in power density term. Furthermore, the housing and components of smartphones are taken into our consideration in this paper.

INDEX TERMS Dual polarized, MIMO, 5G, metasurface, characteristic mode analysis, and mobile handset antenna.

I. INTRODUCTION

Nowadays, the communication systems have been developed rapidly and attract the researchers due to its new features such as high data rate, wide bandwidth, high resolution, heterogeneous services, virtual networks, provide hugely broadcasting data, and fast action. One of these communication systems is the new cellular generation that is called the fifth generation (5G) [1], [2]. The 5 G system has been planned to provide a gold key to the quickly growing demand for mobile data traffic (data rate), overcoming the constraints of the present capability of communication technologies. Therefore, the International Telecommunication Union (ITU) has established several groups to achieve all 5G standards before 2020 and the ITU release the applicable frequencies for the new mobile generation (5G) between 24 GHz and 86 GHz [3]. Even though the range of 5G still under review,

The associate editor coordinating the review of this manuscript and approving it for publication was Giorgio Montisci.

there are several candidate bands [4]. There are different bands such as sub 3 GHz, sub 6 GHz and millimeter bands that are recommended for 5G applications. But many of researchers selected the millimeter bands because the low frequency bands are crowded and overloaded by different applications, therefore the low frequencies can't meet the required broadband of the 5G [1], [5]–[15]. The range from 28 GHz to 38 GHz is highly recommended [16]. The antenna is considered as a mastering key for this new communication system. In order to design an effective antenna for 5G mobile phone, there are several fundamental challenges that need to be considered; one of these challenges is the free space loss (FSL) and atmospheric absorption (AA) that have large values due to the higher frequency of millimeter ranges. To solve the problems of high losses in MM-wave, substantial efforts have been introduced to design 5G antennas with high gain, small size and novel geometry such as patch [11], slot [14], [17], phased arrays [18], switchable antennas [6], and dipole antenna arrays [19] are presented for miniature the

antenna size. All the aforementioned designs are presented for miniaturizing the antenna size but they have their own constraints such as feeding network loss, low gain, and the complexity of the structures.

Nevertheless, most of the antennas in this range are limited to the linearly polarized antennas, while in the real case the mobile terminal will encounter different sorts of movements in Euler areas in addition to the characteristic loss in the millimeter bands. Therefore, the miss polarization among the transmitter and the receiver antennas is one of the main significant loss factors in this communication system. For full utilization of power in 5G systems, the antenna of dual-polarization is a good candidate for solving the problems of power losses and increase the bit data rate of the communication systems [20]. So, the antenna with different polarization (polarization diversity) plays an essential key to solve the aforementioned problems.

In [21] Yang Li *et al.*, introduce a hybrid eight ports orthogonal dual-polarized antenna for 5G smartphones, this antenna consists of 4 L-shaped monopole slot elements and 4-C-shaped coupled fed elements. The 4 L-shaped are printed at the corners and the 4 C-shaped are printed at the middle of a thick 1mm FR-4 substrate. This design achieves 12.5 dB, 15 dB for the isolation and the cross-polarization, respectively. Through the past months, Zaho *et al.* [22] present a dual-polarized antenna for 5G/WLAN based on the integration between inverted cone monopole antenna and cross bow-tie antenna for VP and HP, respectively. The cross bow-tie antenna is fed by a 90° phase difference feeding network. Therefore, the separated power divider and phase shifter are used as a feeding network. In [23] Huang *et al.* introduce a dual-polarized antenna that consists of a main radiator, an annulus, and a reflector. The main radiator consists of two pairs of differentially-driven feedlines to transmit the energy to the coplanar patch. This structure achieves 26 dB and 35dB for the isolation and the cross-polarization, respectively. Eight-ports dual-polarized antenna array is reported in [24], the proposed antenna array is composed of four square loops and each loop is excited by two orthogonal fed coupled feeding strips.

The multiple-input-multiple-output (MIMO) system is preferred for 5G smartphone applications to meet the high demand for maximizing the throughput and the quality of service. In other words, the MIMO antenna technology is one of the most significant components of future wireless communication schemes as it improves throughput without raising the input power and the bandwidth. However, the incorporation of the MIMO antenna scheme into the same board for handheld devices that have a small size is challenging owing to the high mutual coupling between the adjacent antenna components, particularly when they are spaced less than a half-wavelength apart [25]–[28].

To address the aforementioned problems and challenges/limitations, this article recommends a compact dual-polarized MIMO antenna for handheld 5G devices. The dual-polarization is introduced due to its mastering
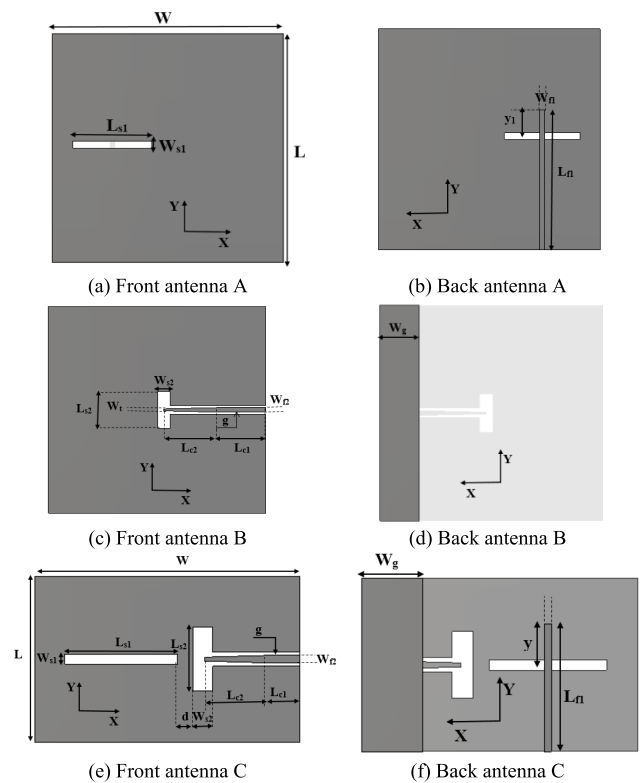

FIGURE 1. Geometry of the proposed antenna.

performance in introducing a solution to improve the spectral efficiency, to enhance the isolation and to enlarge channel capacity. In addition to use of metasurfaces to improve the gain of the proposed antenna. The proposed design consists of two slot antenna: the first is a slot antenna with bottom microstrip feed line and the second is a co-planar slot antenna with CPW feed on the top layer. The 5G design operates at 28 GHz with dual-polarization and achieves high isolation between ports 43dB and cross-polarization (40 dB). The proposed structure has a peak realized gain (5-6 dBi), and radiation efficiency (85-95%). The proposed antenna based on the characteristics mode analysis /theory of characteristics mode is introduced. The MIMO antenna consists of 8 ports to serve the high data rates and the channel capacity of the 5G.

II. ANTENNA DESIGN AND ITS PERFORMANCE
A. ANTENNA CONFIGURATION
The proposed antenna consists of two orthogonal slots to achieve pure dual-polarization and to give two diversity patterns as shown in Figure 1. The antenna is implemented on a Roger 4003C substrate with a dielectric constant of 3.38, tangential loss of 0.0027 and a thickness of 0.2 mm. The thin substrate is selected to reduce the losses at millimeter band and to be compatible with the end launch connector (1.85 mm) that has a very thin pin.

The slot antenna is one of the popular antennas that is used for smartphones in last few years [1], [29]–[34] due to its simple structure and its multiple operating modes. Figure 1 (a and b) shows the proposed slot Ant. I. The slot is

TABLE 1. Parameters of the proposed antennas (mm).

Parameters	An. I	Ant. II	Ant. III
L	20	20	10
W	20	20	20
L_{s1}	5	---	5
W_{s1}	0.6	---	0.6
Y_1	1.6	---	1.6
W_{f1}	0.428	---	0.428
L_{f1}	11.6	---	6.6
L_{s2}	---	3.8	3.7
W_{s2}	---	1.2	1.2
W_{f2}	---	0.425	0.425
W_t	---	0.225	0.225
L_t	---	0.4	0.4
L_{c1}	---	3.5	3.5
L_{c2}	---	4	4
G	---	0.2	0.2
W_c	---	0.45	0.45
W_g	---	3.5	3.5
D	---	---	0.9

(a) current distribution and electric field for Ant. I

(b) Current distribution and electric field for Ant. II

(c) Simulated electric field, Ant. I   (d) Simulated electric field, Ant. II

FIGURE 2. Expected and simulated electric field and current distributions for Ant. I and Ant. II.

(a)   (b)

FIGURE 3. Reflection coefficients of Ant. I at different values of slot length and slot width.

etched on the ground plane that is printed on the top layer and fed by the 50 ohm microstrip line. The feed line is printed on the opposite side of the ground plane to feed the slot antenna. The second antenna (Ant. II) is a slot antenna fed by CPW line as depicts in Figure 1 (c and d). As a result of the thin layer substrate, the width of the CPW-feeding line is wider than the pin of the end-launch connector (The width of CPW feed line without bottom ground is $W_{f2} = 2.5$ mm while the diameter of end-lunch pin is 0.18 mm). Therefore, we used a CPW with a ground plane to decrease the width of CPW-feeding line and to achieve 50-ohm input impedance. After this, the CPW-feeding line is tapered to match the impedance of the slot. The third antenna (Ant. III: proposed antenna) consists of the integration between Ant. I and Ant. II configurations to achieve the dual-polarization from the two antennas. The two feed lines printed on different faces of the substrate as shown in Figure 1 (e and f), furthermore, the feed lines are orthogonal together. Moreover, the two slots are used to prevent the coupling between the two feed lines. TABLE 1 introduces the geometric parameters of the proposed antenna.

B. ANTENNA PERFORMANCE

Figure 2 shows the current and electric field distributions of the slot antennas I and II. In the case of Ant. I, the magnitude of surface current on the ground plane are the strongest above the microstrip line, thus the slot executes the highest disruptive impact of this current. The current is completely impeded near the center of the slot and induces a charge build-up on the long sides of the slot that acts as a capacitor. Moreover, the current near to the parties of the slot bends around its ends to continue to pass and this like the inductor. Therefore,
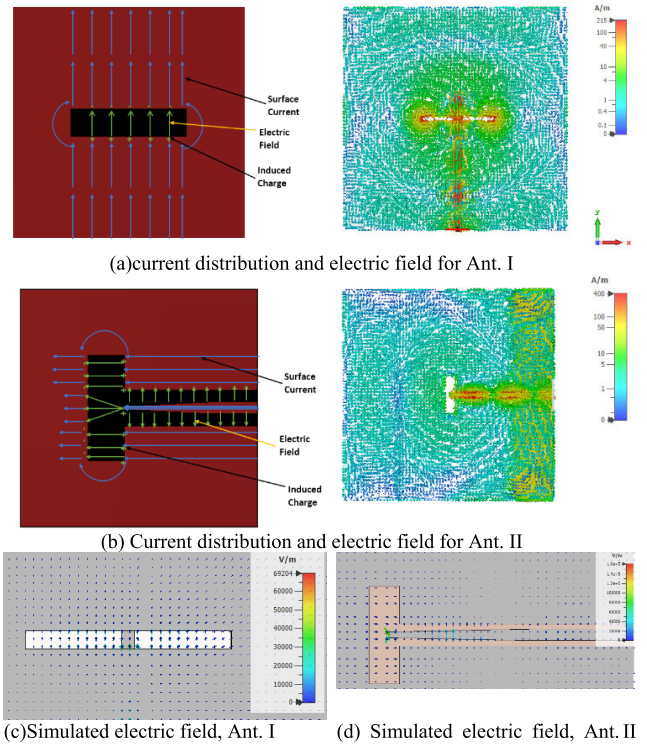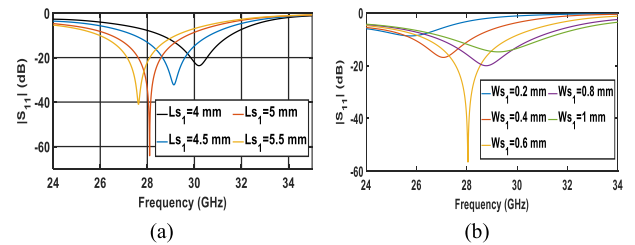
the slot antenna equivalents to two shunt transmission lines shunted by a parallel integration of an inductor and a capacitor. Also, a radiation resistor can be added to the equivalent circuit of slot antenna for long slots.

The proposed slot antenna operates with a length equivalent to $0.5\lambda_g$ from resonant frequency at the center:

$$L_s = \frac{c}{2f_r\sqrt{\epsilon_{eff}}} \quad (1)$$

where L_s is slot length, c is the velocity of free space, f_r is the resonant frequency, and ϵ_{eff} is the relative effective permittivity of the proposed antenna. Figure 3 shows the reflection coefficient of Ant. I at different values of length and width of the slot. For Ant. II, the wide bandwidth is achieved due to the excitation of multiple resonate modes by the combination of the CPW and the slot. The resonant frequency and BW are tuned by the length and width of the slot (L_{s2}, W_{s2}). Figure 4 shows the effect of length and width of the slot on the operating bandwidth.
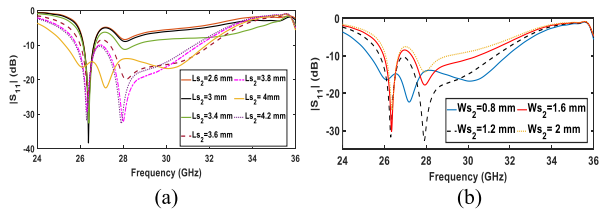
FIGURE 4. Reflection coefficients of Ant. II at different values of slot width and slot length.
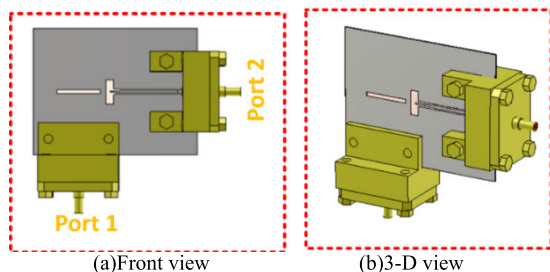

FIGURE 5. Proposed antenna design with connectors.

FIGURE 6. Simulated S-parameters of the two ports antenna.

FIGURE 7. Simulated S-parameters of the two ports antenna (CPW without ground in the bottom).

FIGURE 8. Current distribution of proposed antenna at 28 GHz from two ports.

The polarization of Ant. I is vertical and that of Ant. II is horizontal. W_{s1} and W_{s2} are the dimensions of slots width to control the matching of the vertical and the horizontal modes, respectively. Furthermore, y_0 is a tuning parameter for matching port 1, and W_t, L_t are parameters to optimize the matching at port 2. To consider the practical case, we take the end launch connector into account in our designs as shown in Figure 5. Therefore, length of the feed lines are increased by 5 mm in x and y directions to avoid the interconnection between the two connectors. A high isolation between the two ports can be expected due to the orthogonality characteristics of the two ports and symmetric/ antisymmetric characteristics of the three modes of CPW (with the ground). The reflection coefficients and the isolation coefficients of the proposed antenna are shown in Figure 6. One can notice that the isolation coefficients between the two ports have high values through the operating bandwidth (more than 45 dB) and the antenna has a good matching (S_{11} and S_{22}). The antenna achieves 2.2 GHz as a wide bandwidth from 27 GHz to 29.2 GHz when port 1 is excited and 5 GHz from 25.6 GHz to 31.6 GHz for port 2. The proposed antenna achieved common bandwidth (2.2 GHz) to cover the 5G applications at 28 GHz.

The Ant. III is redesigned without ground in the bottom (the width of CPW line without ground is recalculated) to make the antenna with only one common ground in the top. The S-parameters of this design is shown in Fig. 7. The results are still ensure that the antenna has good matching and high isolation between its ports.

Figure 8 and Figure 9 show the surface current and electric field distributions for the two ports. The surface currents and electric field of the proposed antenna at 28 GHz for the two ports are presented to ensure that the proposed antenna achieves dual-polarization between their ports. It is clear to note that the surface current and the electric field flow along the y-axis when port 1 is fed. While they flow
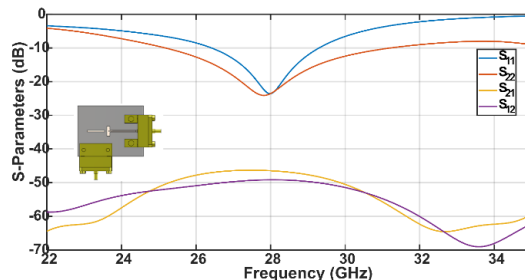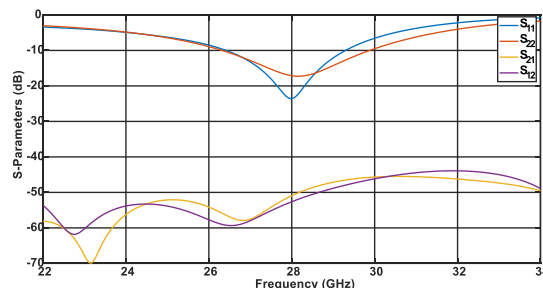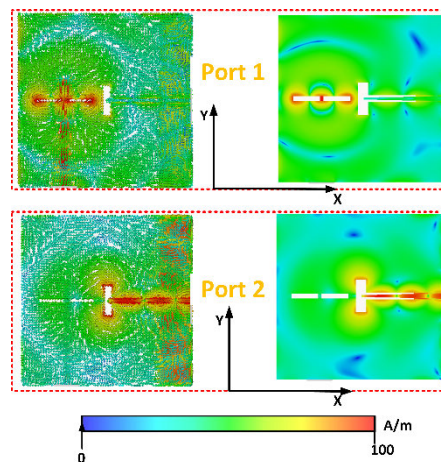
along the x-axis when port 2 is excited. Therefore, dual-polarization is achieved. The radiation patterns of the proposed antenna from port 1 and port 2 in both XZ and YZ planes at 28 GHz are shown in Figure 10. We can observe that the cross-polarization levels in both planes are less than 40 dB as compared with the co-polarizations. The antenna achieves a gain of 6.23 dBi and 6.85 dBi as shown in Figure 11 when excited from port 1 and port 2, respectively.

III. METASURFACE DESIGN AND ANALYZE
A. CHARACTERISTIC MODE ANALYSIS
As described in [35], the characteristics currents are obtained by solving a particular eigenvalue equation that is derived
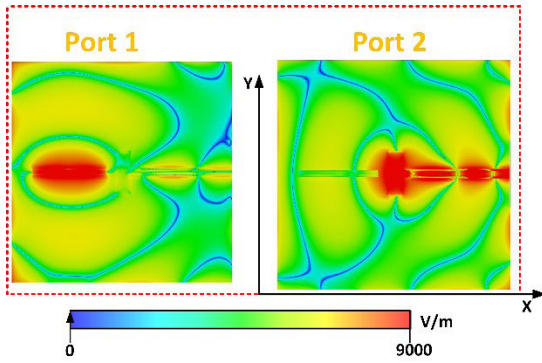
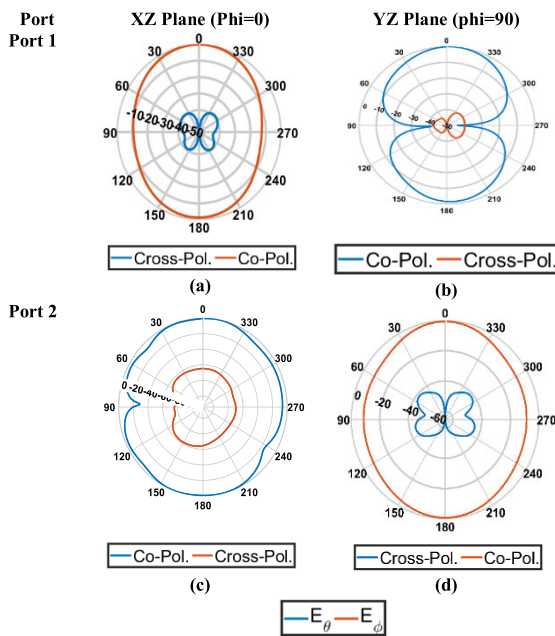**FIGURE 9.** Electric field distributions from two ports.

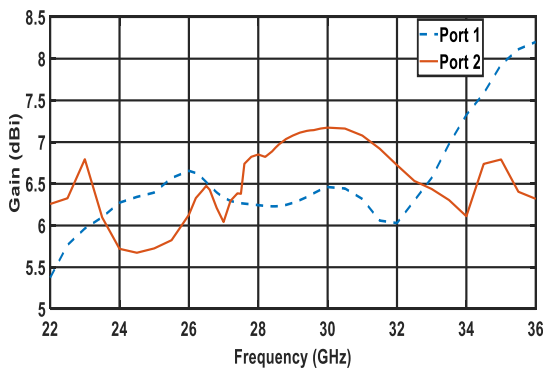**FIGURE 10.** Co-Polarized and Cross-polarized radiation pattern for port1 and port 2 at 28 GHz.

FIGURE 11. Gain of the proposed antenna.

from the Method of Moments (MoM) impedance matrix,

$$Z J = E_{tan}^i \quad \text{where } Z = R + jX \tag{2}$$

From (2), the characteristic modes (CMs) are introduced based on the coefficient matrix's generalized values by Harrington [36]:

$$Z\left(\vec{J}_n\right) = v_n R\left(\vec{J}_n\right) \tag{3}$$

where v_n : eigenvalues, R is a real part of the impedance matrix/operator for the MoM, $\vec{J}_n$ is an eigencurrents (Eigen function) and by noting (2) and (3), the characteristic values can be written in terms of eigenvalues as follows,

$$\lambda_n = \frac{v_n - 1}{j}, \; v_n = 1 + j\lambda_n \tag{4}$$

where λ_n corresponding characteristic values to the eigenvalues. The eigenvalues have a range from $-\infty < \lambda_n < +\infty$. To solve the MoM equation, the CMs are used as a basis function to expand the unknown total current, J, on the surface of the metal as

$$J = \sum_n \frac{V_n^i J_n}{1 + j\lambda_n} \tag{5}$$

where V_n^i is the excitation coefficient on the conductor surface. The excitation coefficient can be expressed as

$$V_n^i = \sum_n E^i J_n \tag{6}$$

where E^i is the impressed E-field.

The first step to the analysis of the CMs is to analyze the eigenvalues because they introduce the data on how the related modes (J_n) radiate and how they are related to the resonance. Therefore, the eigenvalues are used as an indicator to know the resonant frequency for each characteristic mode.

The second parameter for CMA is the characteristic angle (α_n):

$$\alpha_n = 180^0 - tan^{-1}\left(J_n\right) \tag{7}$$

The characteristic angle calculates the difference in phase between the characteristic currents (J_n) and its related characteristic fields. The characteristic angles values are within the range $0^0 \leq \alpha_n \leq 360^0$.

The third parameter for CMT is a model significance (MS):

$$MS_n = \left| \frac{1}{1 + j\lambda_n} \right| \tag{8}$$

This term represents the inherent normalized amplitude for each current mode J_n and it is named the modal significance. If its value close to 1, the mode meets the resonance condition. From MS equation (8), we are able to calculate the resonance of the CM in addition to the operating bandwidth of CM. The CM that has a resonance must be at $\lambda_n = 0$ and $MS_n = 1$ and the CM that doesn't contribute to the radiated field is at $MS_n = 0$.

The multilayer solver and integral equation solver from CST Microwave Studio are chosen to implement the CMT with very high quality [37]–[39]. These solvers are used to calculate the characteristic modes and those related parameters.
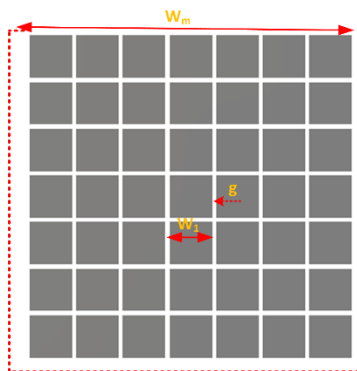
FIGURE 12. Metasurface structure (W1 = 1.7 mm, g = 0.2 mm, Wm = 13.3 mm).

B. DESIGN OF METASURFACE (MTS)

In this section, the analysis of MTS and the integration between MTS and antenna are introduced. The MTS of 7×7 unit cells (square patches) is proposed at 28 GHz as shown in Figure 12. The square patches are printed on Rogers RO 4003C substrate with a dielectric constant of 3.38 and a thickness of 0.2 mm. The CMA solver from CST Microwave Studio is used with free space boundary conditions to analyze this structure. To examine the metasurface modal behaviors, the first ten modes are calculated (Eigenvalues, characteristic angles, and modal significances) in the range from 18 GHz to 38 GHz as shown in Figure 13 (a)-(c). Over the band, we notice that only the modes from 1 to 9 that have resonant frequencies are appeared. In this design, the vertical and horizontal polarizations are desired. Therefore, we need two similar modes (one is VH and the other is HP) over the proposed band. In this design, we have two groups of degenerate modes (J_1/J_2 and J_7/J_8) that can be used, but the other modes are not considered according to (6). On the other hand, J_7/J_8 are at the end of operating band (31 GHz). Figure 13 (a)-(c) shows that the mode J_1/J_2 are the only two modes that have pure resonant at 28 GHz. Also, $J_1 \backslash J_2$ have characteristic angle equal to 180^0 at 28GHz in addition to zero Eigenvalue at 28GHz.

The modal electrical surface currents are shown in Figure 14 (a) and the current directions of each mode are indicated by black arrows. All the fields and currents in this section are calculated at 28 GHz. As can be noticed, first modal current (J_1) is in phase through the MTS and its polarization in the y-direction. Also, the second modal current (J_2) is typical as (J_1) but with 90^0 out of phase. In other words, J_2 is directed in the x-direction through the MTS. Therefore, J_1/J_2 are a pair of orthogonal modes. As a result of that all currents of the first and the second modes are in phase, they have pure broadside radiation as shown in Figure 14 (b). J_3 and J_5 have symmetrical distribution about y-axis, and x-axis, respectively with null current at the center of MTS and a null along z-axis in the radiation pattern as shown in Figure 14 (b). The current of the third mode (J_3) flows as a closed loop with null at the center and thus it looks like the behavior of inductor, which can be verified from its
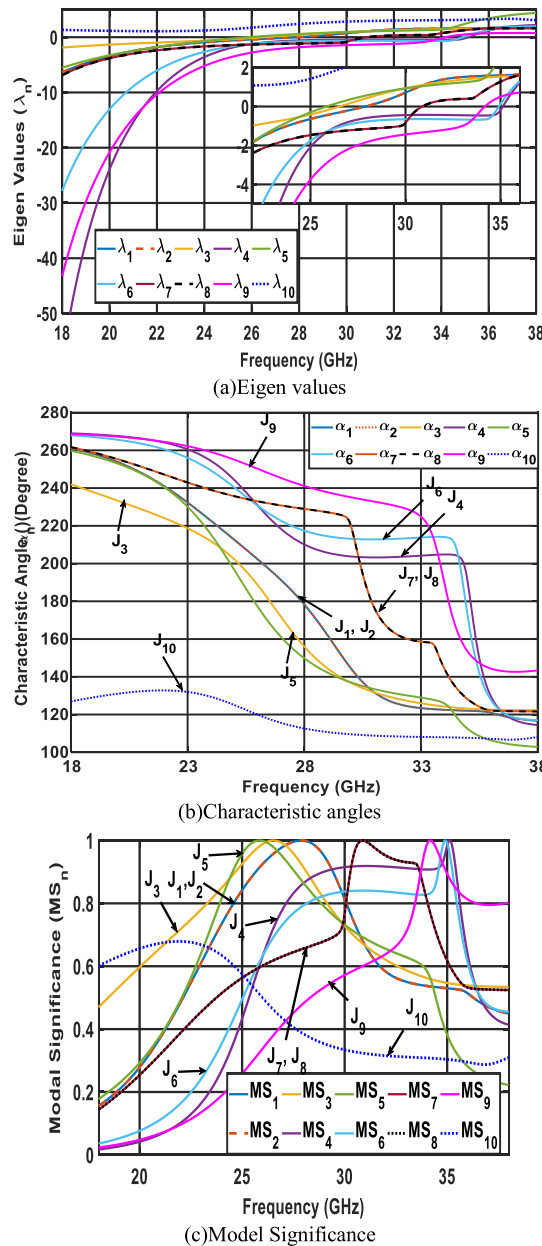

(a)Eigen values

(b)Characteristic angles

(c)Model Significance

FIGURE 13. CMA parameters of MTS.

characteristic angle at about 28 GHz is being below 180^0. The currents of mode J_4 and mode J_6 are self-symmetrical about y and x axis, respectively. J_7 and J_8 are 90^0 out of phase and symmetrical around 45^0 from x-axis and y-axis, respectively. The last two modes have quasi-quadrature symmetric about x-axis and y-axis at the same time. Clearly, the only modes J_1 and J_2 have good main lobe whereas the others modes have split main lobes. Therefore, these are unacceptable modes according to (6) and the theory of mode expansion.

IV. ANTENNA DESIGN WITH MTS

In this section, the MTS is used to provide high gain, wide bandwidth, and compact size and to reduce the back radiation
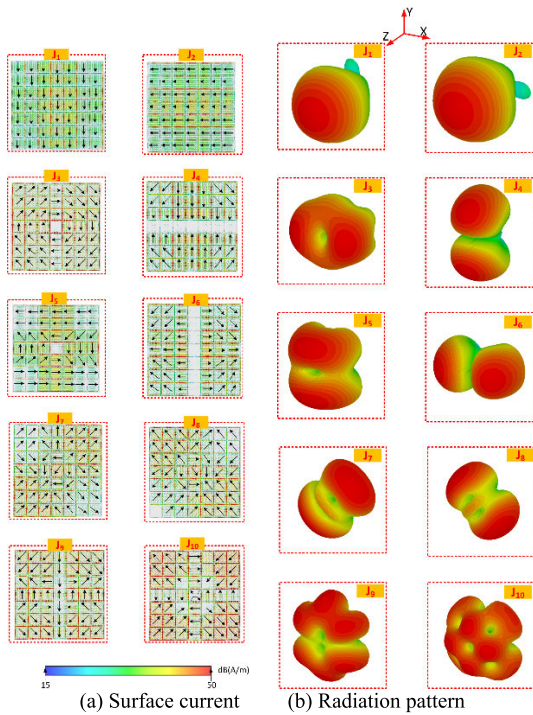
(a) Surface current   (b) Radiation pattern

FIGURE 14. Modal surface current and radiation pattern of MTS at 28GHz.

(a)3-D structure   (b)Top view

(c)MTS layer

(d)Slots layer   (e)Bottom layer

FIGURE 15. Configuration of proposed antenna with MTS.

TABLE 2. Dimensions of the proposed mts antenna (mm).

L	W	L_{s1}	W_{s1}	Y_1	W_{f1}	L_{f1}	L_{s2}	W_{s2}	W_t	L_t	L_{c1}
20	20	4.8	0.6	1.6	0.428	6	3.2	1.1	0.21	0.4	3
L_{c2}	G	W_c	W_g	d	W_m	W_1	g_m	W_{m1}	W_{m2}	L_{m1}	L_{m2}
3.5	0.2	0.45	3.5	0.9	13.3	1.7	0.2	0.4	1	4.8	3.2

(a)Front view   (b)Back view
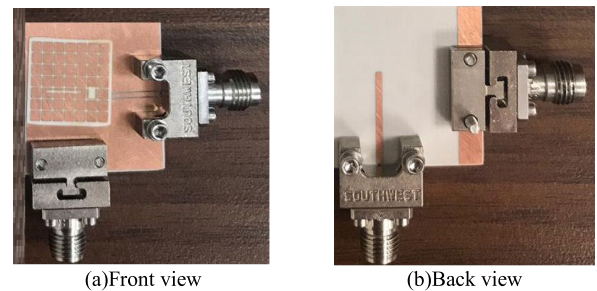
FIGURE 16. Prototype of proposed antenna with MTS.

from the slot antenna. The integration between the proposed antenna and MTS is as following:

- The dual polarized antenna is based on two slots are introduced to operate at 28 GHz (in section II).
- Then we optimize the dimensions of metasurface unit cell to have the pair of orthogonal modes (J_1-J_2) with broadside radiation. Moreover, the others modes of MTS are out of the focused band and they have spilt main lobe (in section III A).
- In this section, the integration between the dual slots antenna and the MTS is introduced. The slots that are adjusted to operate at 28 GHz are used to excite the modes J_1 and J_2 of the MTS that have pure resonant at 28 GHz.

The MTS is feed by the two slot antennas to excite the first and second modes of MTS at 28 GHz. Therefore, the two small slots are etched from the MTS and aligned to the slots of the antenna to increase the coupling between the antenna and the MTS. Figure 15 depicts the configuration of the proposed antenna with MTS layer. The optimized dimensions of the antenna after integration with MTS are shown in TABLE 2. The overall dimensions of the antenna are extended by 5 mm in x and y directions to be compatible with the end launch connector (1.85 mm). The proposed antenna is printed on Rogers 4003C with a dielectric constant of 3.38 and a thickness of 0.2 mm. The prototype of the proposed antenna is shown in Figure 16.

Figure 17 shows the measured and simulated reflection coefficients and isolation coefficients of the ports for the proposed antenna. The measured operating frequency of the
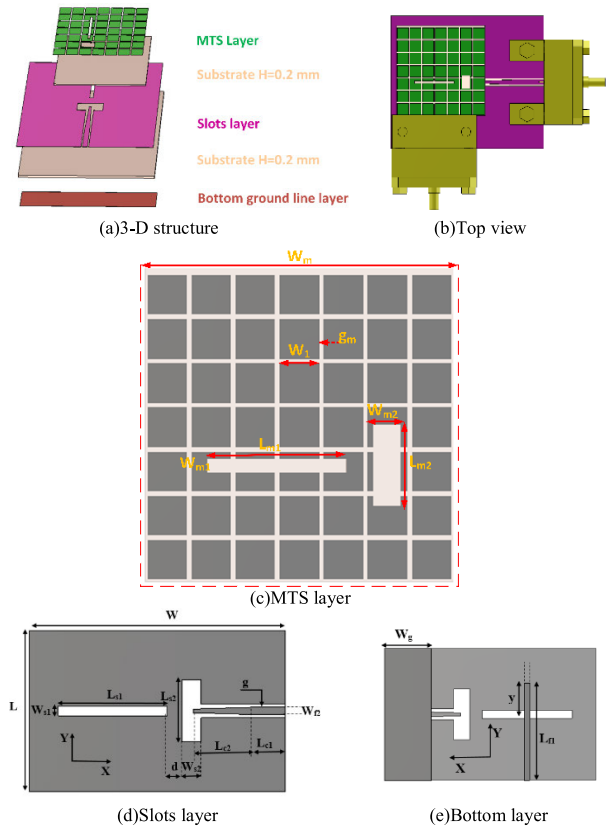
proposed antenna is 28 GHz which in good agreement with the simulated results. The results confirmed that the proposed antenna achieves wide bandwidth from two ports that satisfy the requirements of the 5G communications in terms of bandwidth. The proposed antenna achieves good isolation between its ports (more than 40 dB). The normalized radiation patterns of the MTS antenna are shown in Figure 18 for port 1 and port 2 in the x-z plane and the y-z plane at 28GHz. The co- and cross-components are introduced with more than
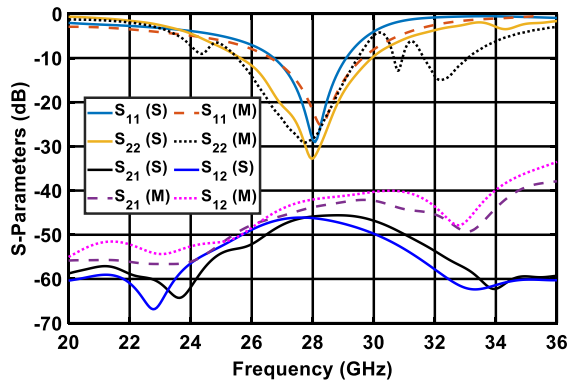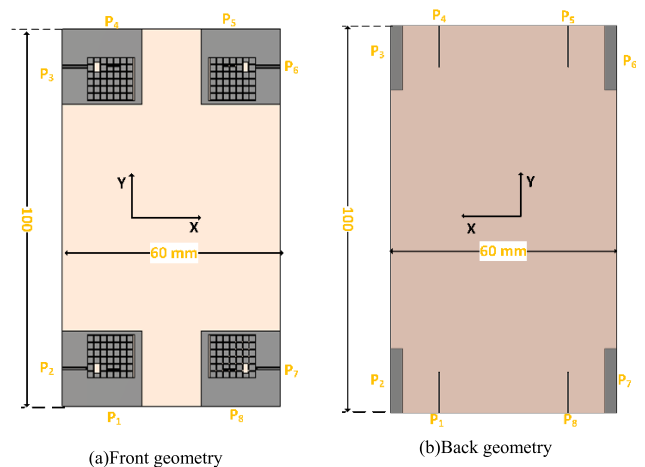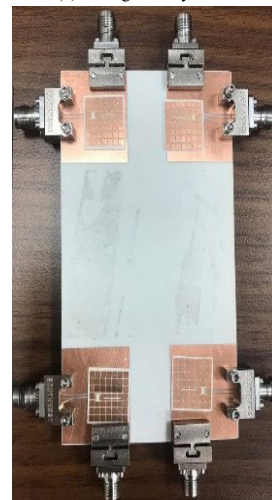
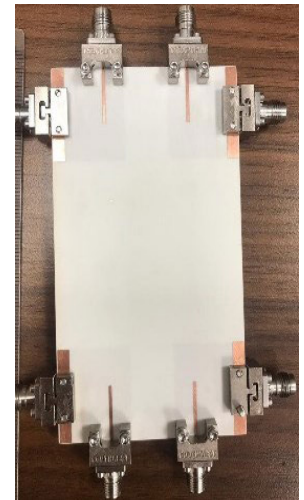**FIGURE 17.** Simulated and measured S-parameters of single antenna (Ports 1 and 2).

FIGURE 18. Co-Polarized and Cross-Polarized radiation pattern for port 1 and port 2 of MTS antenna.

(a)Front geometry　　　(b)Back geometry

(c)Front photo　　　(d)Back photo

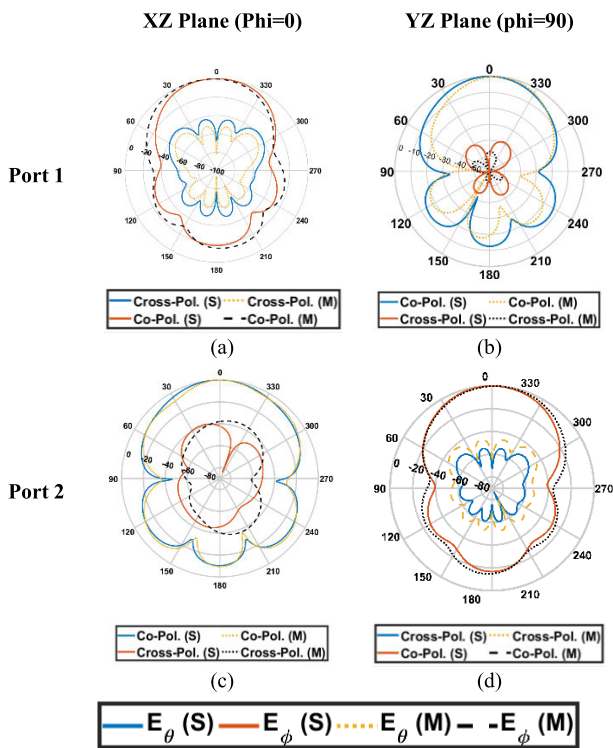**FIGURE 19.** MIMO configuration and prototype of proposed antenna with MTS.

(a)Simulated　　　(b)Simulated

(c)Measured　　　(d)Measured

FIGURE 20. S-parameters of the proposed antenna with MTS.

40 dB between them. Furthermore, the MTS achieved low back radiation at the two ports in the x-z plane and the y-z plane.

V. MIMO ANTENNA DESIGN

In our proposed MIMO antenna, the antenna elements are positioned at the corners of the handset board with a total dimensions of 100×60 mm^2 as shown in Figure 19 for the design configurations and prototypes of the MIMO antenna with MTS. The simulated and measured reflection coefficients of the 8 ports MIMO antenna are introduced in Figure 20 (a and c) in order to ensure that the MIMO antenna has more than 2GHz bandwidth shared between its
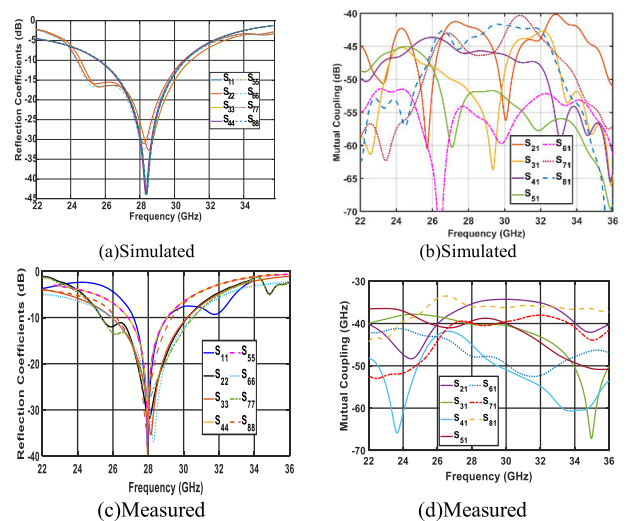
ports. The isolation coefficients related to port 1 are introduced in Figure 20 (b and d). One can notice that the worst isolation coefficient is higher than 36 dB between port 1 and
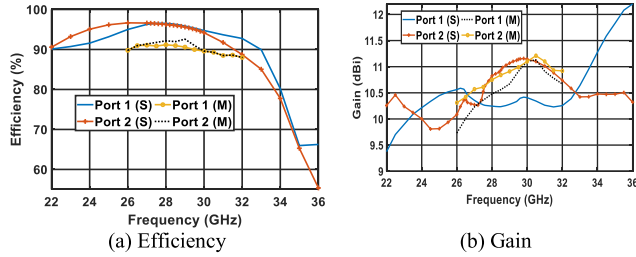
FIGURE 21. Simulated and measured radiation characteristic of the proposed antenna.
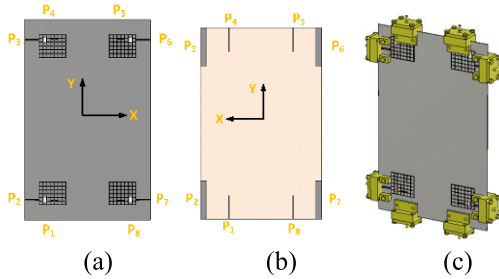

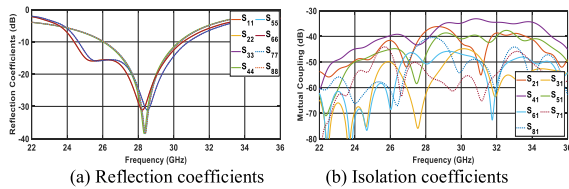FIGURE 22. The configuration of MIMO antenna with common ground (a)Front view, (b)Back view and (c)3-D view.

FIGURE 23. S-parameters of proposed MIMO antenna with common ground plane.

FIGURE 24. ECC parameter of the proposed antenna with MTS.

port 2 in the measured case and more than 40 dB in the simulated case. The simulated and measured reflection coefficients of proposed antenna achieve wide bandwidth from two ports (26-30 GHz for port 1 and 25– 30 GHz for port 2) with shared bandwidth more than 3 GHz between all ports.

The radiation efficiency of the two ports are illustrated in Figure 21 (a). The efficiency of the proposed MTS antenna is around 92% within the whole band. The gain of the proposed antenna is shown in Figure 21 (b), one can notice that the MTS is used to increase the gain of the proposed antenna and to achieve a gain of 11 dBi. The results from other ports are similar to port 1 and port 2.

Some of the antennas in smartphones require a common ground plane between its MIMO elements. Therefore, the MIMO antenna with printed common ground plane on the top layer is presented in Figure 22. The common ground plane does not have any significant changes on the reflection coefficients of the MIMO elements, in contrast, it reduces the isolation between ports by small significant amount as shown in Figure 23. One can notice that the worst isolation coefficient is higher than 37 dB between port 1 and port 2.
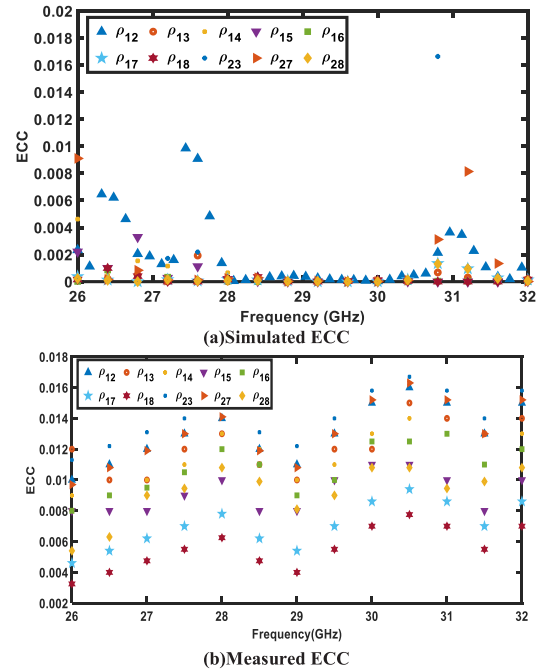
Furthermore, all ports have good matching and achieve the required BW for 5G applications.

The envelope correlation coefficient (ECC) is one of the main parameters to evaluate the MIMO performance. The ECC is used to calculate the similarity between the antenna performances and to evaluate the diversity between the elements of MIMO. The acceptable value of ECC should be less than 0.5 [25]–[28]. Whereas the lower values of ECC mean that each of the two antennas are good isolated. The ECC can be calculated based on the radiation pattern as:

$$\rho_{mn} = \frac{\left| \iint_0^{4\pi} \left[\vec{F}_m(\theta, \varnothing) \times \vec{F}_n(\theta, \varnothing) \right] d\Omega \right|^2}{\iint_0^{4\pi} \left| \vec{F}_m(\theta, \varnothing) \right|^2 d\Omega \iint_0^{4\pi} \left| \vec{F}_n(\theta, \varnothing) \right|^2 d\Omega} \quad (9)$$

where ρ: ECC, $F(\theta, \varnothing)$: radiation patterns of antenna #m or #n, m and n are number of the antenna m,n = 1,2,. . .,8.

Figure 24 shows the different ECC values between the MIMO elements (two elements each time) based on the 3-D radiation pattern of each element. The values of ECC is very small due to the different polarization between the neighbour antennas. It is observed that the values of ECC is less than 0.02 and this means that the MIMO antenna has a good diversity performance.

VI. SMARTPHONE MODELING
A. IMPACTS OF HOUSING AND PHONE COMPONENTS
To simulate the real environment of the smartphones, the antenna is integrated with the housing and the components of mobile as shown in Figure 25. The screen, speaker, camera, battery, and other components are considered with the proposed MIMO antenna and all components are covered
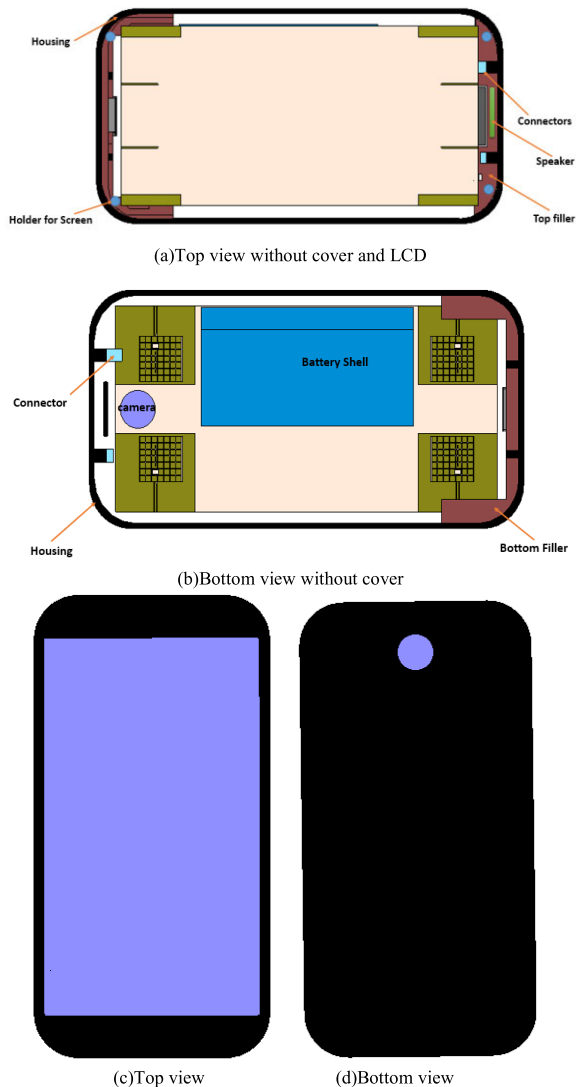
(a)Top view without cover and LCD

(b)Bottom view without cover

(c)Top view   (d)Bottom view

FIGURE 25. Mobile modeling with the components.

TABLE 3. Materials of smartphones.

Part	Material	Properties
Housing	Plastic	ε_r=2.2, $tan\delta$=0.005
Camera	Glass(Pyrex)	ε_r=4.82, $tan\delta$=0.0054
LCD shield	Metal(Copper)	σ=5.8e7 (S/m)
LCD panel	Glass(Pyrex)	ε_r=4.82, $tan\delta$=0.0054
holder	Plastic	ε_r=2.2, $tan\delta$=0.005
Connectors	Plastic	ε_r=2.2, $tan\delta$=0.005
Battery cell	Metal(Copper)	σ=5.8e7 (S/m)
Battery shell	Plastic	ε_r=1.5
Filler	Plastic_HDPE	ε_r=2.3
Speaker	Plastic	ε_r=2.2, $tan\delta$=0.005
Antenna PCB	Rogers 4003C	ε_r=3.38, $tan\delta$=0.0027

*HDPE: High Density Polyethylene

by plastic material. The materials of each part are tabled in TABLE 3. The module of liquid crystal display (LCD) consists of two parts; the LCD panel and the LCD shield that have the same size of PCB. The battery cell is placed
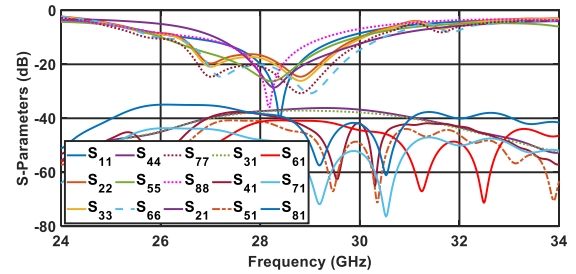
FIGURE 26. S-Parameters of the proposed MIMO antenna inside housing.
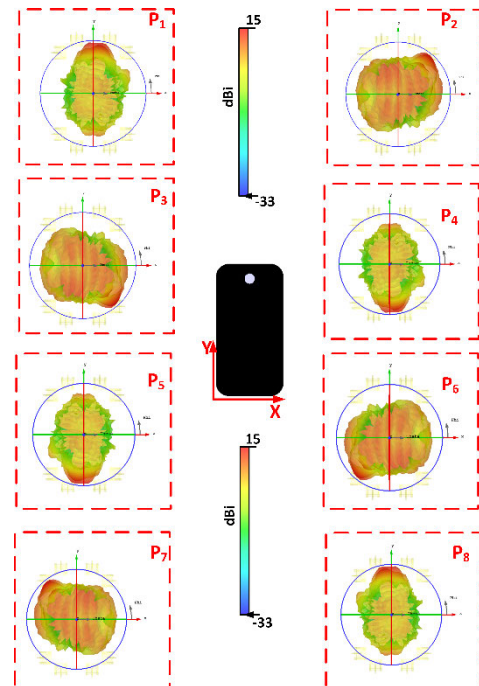
FIGURE 27. 3-D radiation pattern of all ports at 28 GHz (with housing).

inside the battery shield as shown in Figure 25. There are top and bottom fillers to fix the board. Four plastic holders are used to fix the LCD panel and the LCD shield on the filler. The dimensions of all components are compatible with commercial smartphones. The MIMO antenna is tested inside the phone taking the housing and the components into considerations. The S-parameters of the proposed antenna are shown in Figure 26. One can notice that the reflection coefficients from all elements are affected due to the existence of the housing. The reflection coefficient of the ports are slightly shifted but are still have good matching and achieve the requirements for millimeter 5G. On the other hand, there is a high isolation between ports. The 3-D radiation patterns of MIMO elements are presented in Figure 27. We can notice that the radiation patterns are in different directions due to the diversity between the elements.

B. IMPACTS OF HUMAN HEAD
The research on health risk from the electromagnetic waves produced from wireless terminals is introduced in the

FIGURE 28. SAR distribution from MIMO elements.

TABLE 4. Sar values (w/kg).

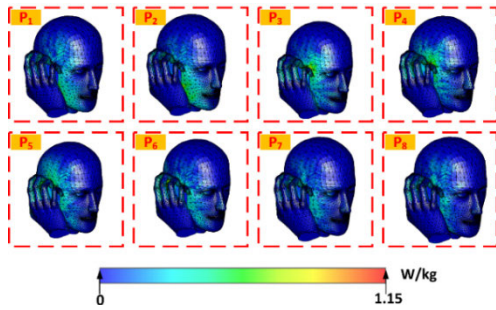| Port		1	2	3	4	5	6	7	8
SAR (1g)	NH	0.69	0.71	0.64	0.73	0.75	0.78	0.67	0.67
	H	0.24	0.28	0.19	0.28	0.3	0.31	0.19	0.15
SAR (10g)	NH	0.48	0.49	0.501	0.52	0.54	0.496	0.57	0.45
	H	0.14	0.14	0.17	0.13	0.15	0.16	0.15	0.11

*H: with housing, NH: without Housing

TABLE 5. Power density limits from different standards.

	ICNIRP [45]	FCC[44]	IEEE[46, 47]	
F(GHz)	10-300	6-100	3-30	30-100
Pd (W/m²), (A)	10, (20 cm²) 200, (1 cm²)	10, (1 cm²)	10, (100 λ^2) 18.56$f^{0.699}$	10, (100 cm²) 200, (1 cm²)

literature. The Specific Absorption Rate (SAR) is a figure of merit for evaluating the power absorbed by the human tissues for the frequencies used by current mobile communications networks of second, third and fourth generation (2 G, 3 G and 4 G) [40]–[43]. The SAR quantifies are the absorbed energy per unit tissue volume and the SAR values should follow one of two standards: American standard (1.6 w/kg) for each 1 g or European standard (2 w/kg) for each 10g [44]–[47].

For the millimeter wave range, there are two approaches to calculate the electromagnetic exposure to the human:

1) SAR: Some papers in the literature evaluate the electromagnetic exposure by the same previous definition of SAR [5].

2) Power density: the term to calculate the electromagnetic exposure into the human body changed from SAR to the term of power density (Pd) because the absorption becomes more superficial due to the fact that penetration is very low at higher frequencies [48]–[51].

Figure 28 shows the distribution of SAR from 8 elements for 10g standard. The SAR values for the two standards are summarized in TABLE 4. The antenna is proximity close to the human head model with 0.5 mm distance and inclined as in the take mode by (60⁰). The reference power of the proposed antenna elements at 28 GHz is set to 24 dBm for each element.

TABLE 6. Power density values at 28 GHz from different ports according to different standards.

Power density (Without Housing) W/m²								
Port	1	2	3	4	5	6	7	8
ICNIRP	1.32	1.32	1.35	1.32	1.28	1.25	1.35	1.35
FCC	1.97	1.96	1.99	1.99	1.98	1.98	1.97	1.97
IEEE	1.71	1.69	1.78	1.77	1.68	1.69	1.71	1.71
Power density (With Housing) W/m²								
Port	1	2	3	4	5	6	7	8
ICNIRP	0.85	0.85	0.85	0.83	0.82	0.79	0.72	0.86
FCC	1.1	1.12	1.12	1.05	1.03	0.97	0.99	1.21
IEEE	1.0	0.97	1.21	1.11	1.11	1.11	1.15	1.16

(a)Reflection coefficient   (b)Mutual coupling
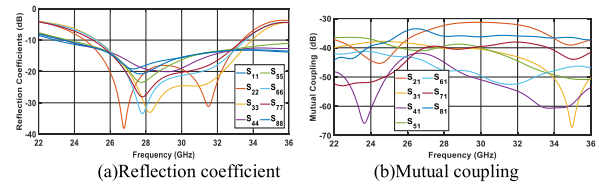
FIGURE 29. S-parameters of proposed MIMO antenna with mobile modeling (with head and hand).
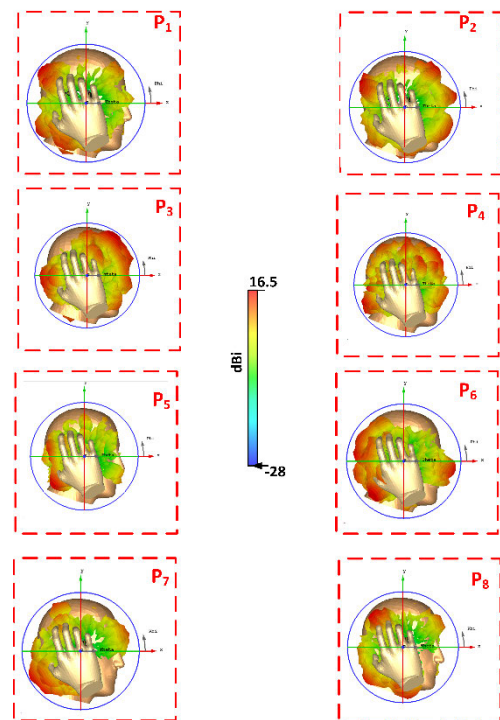
FIGURE 30. 3-D radiation patterns of MIMO elements (with head and hand).

In the second approach, IEEE, FCC and International Commission on Non- Ionizing Radiation Protection (ICNIRP) introduced frequency limits at which the definition of SAR calculation shifts to power density calculation as shown in TABLE 5. The conversion frequency at which this shift in exposure metric is 3 GHz, 6 GHz and 10 GHz, for IEEE, FCC, and ICNIRP, respectively. In other

TABLE 7. Comparison between referenced antennas and the proposed antenna.

Ref	Size (λ_0^3)	Isolation (dB)	Gain (dBi)	X-pol (dB)	Freq. (GHz)	Eff. (%)	Complicated	Remarks
[52]	1.37×1.37×0.222	39	13	42	8.16-11.15	NA	High	• Six layers. • Based on integrated cavity.
[53]	3.2×3.2×0.1	20	3.8	25	30.1-30.9		High	• Multilayer organic buildup substrates.
[54]	1.75×1.75×0.02	35	8.6	20	2.4-4.12	NA	Medium	• Two substrates • Dual-pol. • Circular dipole • Microstrip line Balun feed
[55]	2.7×2.54×0.10	18	7.48	10	27.5-29.5	NA	High	• SIW horn antenna. • Works as a waveguide antenna. • 3 layers
[56]	1.73×1.03×0.144	30	9.4	20	1.88-2.9	NA	High	• Fed by parallel strip line balun. • Bulk structure • 3 layers
[57]	0.93×0.93×0.004	26	4.5	28	1.86-2.97	NA	High	• H-shaped slot antenna. • 90^0 phase shift feeding network.
Proposed antenna	0.83×0.83×0.03	40	11	40	25.5-30	92	Low	• Low profile • Two orthogonal slots. • Dual feed.

MIMO Antenna for 5G Smartphones								
Ref.	Phone Board (mm²)	H_0 (mm)	MIMO Order	Gain (dBi)	ECC	Isolation (dB)	Dual-Pol. (X.Pol.)	Eff. (%) / Remarks
[21]	136×68	5	8	NA	0.15	12.5	yes (15)	55 — • C-shaped coupled-fed and L-shaped monopole slot.
[58]	150×75	6.2	8	NA	0.08	11	No	42 — • 3-D folded monopole. • Dual band @3.5 GHz, and 5 GHz.
[31]	150×80	0.8	8	NA	0.05	17.5	No	62 — • Open slot antenna
[59]	NA	1.93	8	7	NA	20	Yes (18.3)	90 — • 3 layers. • Yagi-uda • Endfire radiation
Proposed antenna	100×60	0.4	8	11	0.001	40	Yes (40)	90 — • Low profile • Two orthogonal slots. Dual feed.

words, at mm-Wave frequencies, PD is currently preferred due to the difficulty of determining a reasonable volume for SAR assessment when the penetration depths are very low [44]–[47]. The power density exposure into the human model is calculated as shown in

TABLE 6 for all ports and is compared relative to different standards. We noted that all the power densities satisfy the safety guidelines. The SAR values and power density values are recalculated for the smartphone with housing.

For more investigation of the proposed MIMO antenna with the human head and hand, the antenna performance in terms of the S-parameters and the radiation patterns are introduced as shown in Figure 29 and Figure 30, respectively. A server computer with Xeon-Gold 16 cores processor and 128 GB RAM is used to simulate the smartphone with the human head and hand over the required band. One can be observed that the human head and hand have more effect on the matching of the VP antennas (ports 1, 4, 5, and 8) than that of the HP antennas. This variation occurs because the VP antennas are aligned to the length of the mobile phone that has a large area that is touched with the human than that of the antennas that are aligned to the width of the mobile (HP antennas). Even with the changes in the matching of VP antennas but they still have a good impedance bandwidth that covers more than 4 GHz with reference of -10 dB. The isolation coefficients between MIMO elements are larger than 32 dB. In term of radiation patterns, the MIMO antenna with the human model still achieve the diversity between its ports and achieves high gain.

C. COMPARISON
TABLE 7 lists two comparison sections; the first section makes a comparison between the proposed antenna and the referenced dual-polarized antennas and the second section

makes a comparison between the proposed antenna and the referenced MIMO antennas of smartphones One can notice that the dual-polarization in [52]–[56] is achieved based on multi-layers and complex feeding structures. However, the antenna in [57] is designed on a single layer but it has a very complicated feeding network to achieve the dual-polarization. Moreover, the antennas in [53], [57] are with low gain. The proposed dual-slot antenna features the benefits of high gain and wide bandwidth, high isolation, high cross-polarization, low profile and compatibility with dual-polarization for 5G applications compared to previous works. On the other hand, the eight-element MIMO antenna for smartphones are introduced in [21], [31], [58], [59] but all the antennas that are introduced in these papers have thick height except the antenna in [31] that has a thickness of 0.8 mm. The study of the antenna effect on the human body is not introduced in the aforementioned MIMO antennas. Furthermore, these papers achieve low efficiency and low isolation between its ports except the antenna that is introduced in [59] which achieves high efficiency (90%) and accepted isolation between its ports (20 dB). Otherwise, the proposed antenna achieves high isolation between its ports, high gain, high efficiency, and very thin thickness compared to all aforementioned antennas. The proposed work introduces a comprehensive study for all environment of the smartphones and its effect on the antenna performance and vice versa.

VII. CONCLUSION

In this paper, a dual-polarized MIMO antenna with eight elements is introduced for 5G smartphone. The MIMO configuration is based on the diversity between elements. The dual-polarization antenna is introduced to overcome the high attenuation in the 5G communication systems and to give high data rates. Furthermore, the orthogonal-polarization between the antenna ports is used to achieve high isolations between antenna ports. The antenna achieves a good matching bandwidth more than 3 GHz at center frequency of 28GHz. The antenna is combined with MTS to increase its gain and bandwidth. The MTS is analyzed by CMT and all the parameters are investigated. The antenna is fabricated and measured. The electromagnetic exposures into the human model from the proposed antenna at 28 GHz are investigated and analyzed in terms of SAR and power density. High isolation, low profile, low complexity, compact size, high efficiency, high gain, high cross-polarization are achieved in the proposed antenna.

REFERENCES

[1] N. O. Parchin, Y. I. A. Al-Yasir, A. H. Ali, I. Elfergani, J. M. Noras, J. Rodriguez, and R. A. Abd-Alhameed, "Eight-element dual-polarized MIMO slot antenna system for 5G smartphone applications," *IEEE Access*, vol. 7, pp. 15612–15622, 2019.

[2] B. Yu, K. Yang, C.-Y.-D. Sim, and G. Yang, "A novel 28 GHz beam steering array for 5G mobile device with metallic casing application," *IEEE Trans. Antennas Propag.*, vol. 66, no. 1, pp. 462–466, Jan. 2018.

[3] ITU. (2019). *5G—Fifth Generation of Mobile Technologies.* [Online]. Available: https://www.itu.int/en/mediacentre/backgrounders/Pages/5G-fifth-generation-of-mobile-technologies.aspx

[4] J. Zhang, X. Ge, Q. Li, M. Guizani, and Y. Zhang, "5G millimeter-wave antenna array: Design and challenges," *IEEE Wireless Commun.*, vol. 24, no. 2, pp. 106–112, Apr. 2017.

[5] J. Bang and J. Choi, "A SAR reduced mm-wave beam-steerable array antenna with dual-mode operation for fully metal-covered 5G cellular handsets," *IEEE Antennas Wireless Propag. Lett.*, vol. 17, no. 6, pp. 1118–1122, Jun. 2018.

[6] C. Buey, "Design and measurement of multi-antenna systems toward future 5G technologies," Ph.D. dissertation, Univ. Côte d'Azur, Nice, France, 2018.

[7] T. Deckmyn, M. Cauwe, D. Vande Ginste, H. Rogier, and S. Agneessens, "Dual-band (28,38) GHz coupled quarter-mode substrate-integrated waveguide antenna array for next-generation wireless systems," *IEEE Trans. Antennas Propag.*, vol. 67, no. 4, pp. 2405–2412, Apr. 2019.

[8] M. Ikram, R. Hussain, and M. S. Sharawi, "4G/5G antenna system with dual function planar connected array," *IET Microw., Antennas Propag.*, vol. 11, no. 12, pp. 1760–1764, Sep. 2017.

[9] S. Krishna, "Design and development of 5G spectrum massive MIMO array antennas for base station and access point applications," Ph.D. dissertation, San Diego State Univ., San Diego, CA, USA, 2018.

[10] H. G. D. Løvaas, "Multiband UWB antenna design for WiFi, LTE and 5G," M.S. thesis, NTNU, Trondheim, Norway, 2017.

[11] N. Ojaroudiparchin, M. Shen, S. Zhang, and G. F. Pedersen, "A switchable 3-D-coverage-phased array antenna package for 5G mobile terminals," *IEEE Antennas Wireless Propag. Lett.*, vol. 15, pp. 1747–1750, 2016.

[12] S. Salous, V. Degli Esposti, F. Fuschini, R. S. Thomae, R. Mueller, D. Dupleich, K. Haneda, J.-M. Molina Garcia-Pardo, J. Pascual Garcia, D. P. Gaillot, S. Hur, and M. Nekovee, "Millimeter-wave propagation: Characterization and modeling toward fifth-generation systems. [Wireless Corner]," *IEEE Antennas Propag. Mag.*, vol. 58, no. 6, pp. 115–127, Dec. 2016.

[13] A. Zhao and Z. Ren, "Size reduction of self-isolated MIMO antenna system for 5G mobile phone applications," *IEEE Antennas Wireless Propag. Lett.*, vol. 18, no. 1, pp. 152–156, Jan. 2019.

[14] A. A. R. Saad and H. A. Mohamed, "Printed millimeter-wave MIMO-based slot antenna arrays for 5G networks," *AEU - Int. J. Electron. Commun.*, vol. 99, pp. 59–69, Feb. 2019.

[15] M. E. Yassin, H. A. Mohamed, E. A. F. Abdallah, and H. S. El-Hennawy, "Single-fed 4G/5G multiband 2.4/5.5/28 GHz antenna," *IET Microw., Antennas Propag.*, vol. 13, no. 3, pp. 286–290, Feb. 2019.

[16] W. Hong, K.-H. Baek, and S. Ko, "Millimeter-wave 5G antennas for smartphones: Overview and experimental demonstration," *IEEE Trans. Antennas Propag.*, vol. 65, no. 12, pp. 6250–6261, Dec. 2017.

[17] R. Hussain, A. T. Alreshaid, S. K. Podilchak, and M. S. Sharawi, "Compact 4G MIMO antenna integrated with a 5G array for current and future mobile handsets," *IET Microw., Antennas Propag.*, vol. 11, no. 2, pp. 271–279, Jan. 2017.

[18] D. Jackson, "Phased array antenna handbook (third edition) [book review]," *IEEE Antennas Propag. Mag.*, vol. 60, no. 6, pp. 124–128, Dec. 2018.

[19] S. X. Ta, H. Choo, and I. Park, "Broadband printed-dipole antenna and its arrays for 5G applications," *IEEE Antennas Wireless Propag. Lett.*, vol. 16, pp. 2183–2186, 2017.

[20] A. Li, K.-M. Luk, and Y. Li, "A dual linearly polarized end-fire antenna array for the 5G applications," *IEEE Access*, vol. 6, pp. 78276–78285, 2018.

[21] M.-Y. Li, Y.-L. Ban, Z.-Q. Xu, G. Wu, C.-Y.-D. Sim, K. Kang, and Z.-F. Yu, "Eight-port orthogonally dual-polarized antenna array for 5G smartphone applications," *IEEE Trans. Antennas Propag.*, vol. 64, no. 9, pp. 3820–3830, Sep. 2016.

[22] L. Zhao, Z.-M. Chen, and J. Wang, "A wideband dual-polarized omnidirectional antenna for 5G/WLAN," *IEEE Access*, vol. 7, pp. 14266–14272, Feb. 2019.

[23] H. Huang, X. Li, and Y. Liu, "A low-profile, dual-polarized patch antenna for 5G MIMO application," *IEEE Trans. Antennas Propag.*, vol. 67, no. 2, pp. 1275–1279, Feb. 2019.

[24] M.-Y. Li, Z.-Q. Xu, Y.-L. Ban, C.-Y.-D. Sim, and Z.-F. Yu, "Eight-port orthogonally dual-polarised MIMO antennas using loop structures for 5G smartphone," *IET Microw., Antennas Propag.*, vol. 11, no. 12, pp. 1810–1816, Sep. 2017.

[25] P. Gao, S. He, X. Wei, Z. Xu, N. Wang, and Y. Zheng, "Compact printed UWB diversity slot antenna with 5.5-GHz band-notched characteristics," *IEEE Antennas Wireless Propag. Lett.*, vol. 13, pp. 376–379, 2014.

[26] S. Tripathi, A. Mohan, and S. Yadav, "A compact koch fractal UWB MIMO antenna with WLAN band-rejection," *IEEE Antennas Wireless Propag. Lett.*, vol. 14, pp. 1565–1568, 2015.

[27] Y. Li, C.-Y.-D. Sim, Y. Luo, and G. Yang, "12-port 5G massive MIMO antenna array in sub-6GHz mobile handset for LTE bands 42/43/46 applications," *IEEE Access*, vol. 6, pp. 344–354, 2018.

[28] K. R. Jha and S. K. Sharma, "Combination of MIMO antennas for handheld devices," *IEEE Antennas Propag. Mag.*, vol. 60, no. 1, pp. 118–131, Feb. 2018.

[29] Q. Chen, H. Lin, J. Wang, L. Ge, Y. Li, T. Pei, and C.-Y.-D. Sim, "Single ring slot-based antennas for metal-rimmed 4G/5G smartphones," *IEEE Trans. Antennas Propag.*, vol. 67, no. 3, pp. 1476–1487, Mar. 2019.

[30] X. Zhang, Y. Li, W. Wang, and W. Shen, "Ultra-wideband 8-Port MIMO antenna array for 5G metal-frame smartphones," *IEEE Access*, vol. 7, pp. 72273–72282, 2019.

[31] Y. Li, C.-Y.-D. Sim, Y. Luo, and G. Yang, "High-isolation 3.5 GHz eight-antenna MIMO array using balanced open-slot antenna element for 5G smartphones," *IEEE Trans. Antennas Propag.*, vol. 67, no. 6, pp. 3820–3830, Jun. 2019.

[32] M. S. Sharawi, M. Ikram, and A. Shamim, "A two concentric slot loop based connected array MIMO antenna system for 4G/5G terminals," *IEEE Trans. Antennas Propag.*, vol. 65, no. 12, pp. 6679–6686, Dec. 2017.

[33] M. Ikram, N. Nguyen-Trong, and A. Abbosh, "Multiband MIMO microwave and millimeter antenna system employing dual-function tapered slot structure," *IEEE Trans. Antennas Propag.*, vol. 67, no. 8, pp. 5705–5710, Aug. 2019.

[34] L. Liu, C. Liu, Z. Li, X. Yin, and Z. N. Chen, "Slit-slot line and its application to low cross-polarization slot antenna and mutual-coupling suppressed tripolarized MIMO antenna," *IEEE Trans. Antennas Propag.*, vol. 67, no. 1, pp. 4–15, Jan. 2019.

[35] R. Garbacz and R. Turpin, "A generalized expansion for radiated and scattered fields," *IEEE Trans. Antennas Propag.*, vol. AP-19, no. 3, pp. 348–358, May 1971.

[36] R. Harrington and J. Mautz, "Theory of characteristic modes for conducting bodies," *IEEE Trans. Antennas Propag.*, vol. AP-19, no. 5, pp. 622–628, Sep. 1971.

[37] Z.-Y. Zhang, Y. Zhao, N.-W. Liu, L.-Y. Ji, S. Zuo, and G. Fu, "Design of a dual-beam dual-polarized offset parabolic reflector antenna," *IEEE Trans. Antennas Propag.*, vol. 67, no. 2, pp. 712–718, Feb. 2019.

[38] Y. Shi, Z. K. Meng, W. Y. Wei, W. Zheng, and L. Li, "Characteristic mode cancellation method and its application for antenna RCS reduction," *IEEE Antennas Wireless Propag. Lett.*, vol. 18, no. 9, pp. 1784–1788, Sep. 2019.

[39] L. Akrou and H. J. A. D. Silva, "Enhanced modal tracking for characteristic modes," *IEEE Trans. Antennas Propag.*, vol. 67, no. 1, pp. 356–360, Jan. 2019.

[40] K. S. Sultan, H. H. Abdullah, E. A. Abdallah, and E. A. Hashish, "Low-SAR, miniaturized printed antenna for mobile, ISM, and WLAN services," *IEEE Antennas Wireless Propag. Lett.*, vol. 12, pp. 1106–1109, 2013.

[41] H. H. Abdullah and K. S. Sultan, "Multiband compact low SAR mobile hand held antenna," *Prog. Electromagn. Res. Lett.*, vol. 49, pp. 65–71, 2014.

[42] K. S. Sultan, H. H. Abdullah, and E. A. Abdallah, "Low SAR, simple printed compact multiband antenna for mobile and wireless communication applications," *Int. J. Antennas Propag.*, vol. 2014, pp. 1–8, 2014.

[43] K. S. Sultan, H. H. Abdullah, and E. A. Abdallah, "Comprehensive study of printed antenna with the handset modeling," *Microw. Opt. Technol. Lett.*, vol. 58, no. 4, pp. 974–980, Feb. 2016.

[44] *Code of Federal Regulations CFR Title 47, Part 1.1310, Radiofrequency Radiation Exposure Limits*, Federal Commun. Commission, Washington, DC, USA, 1997.

[45] The International Commission on Non-Ionizing Radiation Protection, "Guidelines for limiting exposure to time-varying electric, magnetic, and electromagnetic fields (up to 300 GHz)," *Health Phys.*, vol. 74, no. 4, pp. 494–522, Apr. 1998.

[46] *IEEE Standard for Safety Levels With Respect to Human Exposure to Radio Frequency Electromagnetic Fields 3 kHz to 300 GHz*, IEEE Standard C95.1-2019, 2005.

[47] *IEEE Standard for Safety Levels with Respect to Human Exposure to Radio Frequency Electromagnetic Fields, 3 kHz to 300 GHz Amendment 1: Specifies Ceiling Limits for Induced and Contact Current, Clarifies Distinctions between Localized Exposure and Spatial Peak Power Density*, IEEE Standard C95.1a-2010, 2010.

[48] B. Thors, D. Colombi, Z. Ying, T. Bolin, and C. Tornevik, "Exposure to RF EMF from array antennas in 5G mobile communication equipment," *IEEE Access*, vol. 4, pp. 7469–7478, 2016.

[49] C. Leduc and M. Zhadobov, "Impact of antenna topology and feeding technique on coupling with human body: Application to 60-GHz antenna arrays," *IEEE Trans. Antennas Propag.*, vol. 65, no. 12, pp. 6779–6787, Dec. 2017.

[50] B. Xu, K. Zhao, B. Thors, D. Colombi, O. Lundberg, Z. Ying, and S. He, "Power density measurements at 15 GHz for RF EMF compliance assessments of 5G user equipment," *IEEE Trans. Antennas Propag.*, vol. 65, no. 12, pp. 6584–6595, Dec. 2017.

[51] B. Xu, M. Gustafsson, S. Shi, K. Zhao, Z. Ying, and S. He, "Radio frequency exposure compliance of multiple antennas for cellular equipment based on semidefinite relaxation," *IEEE Trans. Electromagn. Compat.*, vol. 61, no. 2, pp. 327–336, Apr. 2019.

[52] J. Wang, W. Wang, A. Liu, M. Guo, and Z. Wei, "Cross-polarization suppression of a dual-polarized microstrip antenna using enclosed substrate-integrated cavities," *IEEE Antennas Wireless Propag. Lett.*, vol. 19, no. 1, pp. 64–68, Jan. 2020.

[53] D. Liu, X. Gu, C. W. Baks, and A. Valdes-Garcia, "Antenna-in-package design considerations for ka-band 5G communication applications," *IEEE Trans. Antennas Propag.*, vol. 65, no. 12, pp. 6372–6379, Dec. 2017.

[54] C. Wu, C. Lu, and W. Cao, "Wideband dual-polarization slot antenna with high isolation by using microstrip line balun feed," *IEEE Antennas Wireless Propag. Lett.*, vol. 16, pp. 1759–1762, 2017.

[55] J. Zhang, K. Zhao, L. Wang, S. Zhang, and G. F. Pedersen, "Dual-polarized phased array with endfire radiation for 5G handset applications," *IEEE Trans. Antennas Propag.*, to be published.

[56] J. Zhang, X. Q. Lin, L. Y. Nie, J. W. Yu, and Y. Fan, "Wideband dual-polarization patch antenna array with parallel strip line balun feeding," *IEEE Antennas Wireless Propag. Lett.*, vol. 15, pp. 1499–1501, 2016.

[57] C. Wang, Y. Chen, and S. Yang, "Bandwidth enhancement of a dual-polarized slot antenna using characteristic modes," *IEEE Antennas Wireless Propag. Lett.*, vol. 17, no. 6, pp. 988–992, Jun. 2018.

[58] J. Guo, L. Cui, C. Li, and B. Sun, "Side-edge frame printed eight-port dual-band antenna array for 5G smartphone applications," *IEEE Trans. Antennas Propag.*, vol. 66, no. 12, pp. 7412–7417, Dec. 2018.

[59] Y.-W. Hsu, T.-C. Huang, H.-S. Lin, and Y.-C. Lin, "Dual-polarized quasi Yagi–Uda antennas with endfire radiation for millimeter-wave MIMO terminals," *IEEE Trans. Antennas Propag.*, vol. 65, no. 12, pp. 6282–6289, Dec. 2017.

KAMEL S. SULTAN (Student Member, IEEE) received the B.Sc. degree in electronics and electrical communication engineering from the University of Menofia, in 2009, and the M.Sc. degree from Cairo University, in 2014. He was an Assistant Researcher with the Electronics Research Institute (ERI), Cairo, Egypt, from 2010 to 2015. He was a Research Assistant with the Zewail City for Science and Technology, Giza, Egypt, from 2015 to 2018. He back again to ERI, in December 2018. His main research interests are automotive radar antennas, biomedical application, microwave imaging, the design and implementation of low SAR handset antennas, antenna arrays, dielectric resonator antennas, microwave devices, and feeding networks. He was a member of four projects funded from different funding agencies through last eight years.

HAYTHEM H. ABDULLAH received the B.Sc. degree in electronics and communication engineering from the University of Benha, Egypt, in 1998, and the M.Sc. and Ph.D. degrees from Cairo University, in 2003 and 2010, respectively. His M.Sc. is dedicated in the simulation of the dispersive materials in the Finite Difference Time Domain numerical technique and its application to the SAR calculations within the human head. The Ph.D. is dedicated to the radar target identification.

He is currently an Associate Professor and the Head of the Nanotechnology Laboratory, Electronics Research Institute (ERI), Cairo, Egypt. His current research interests are design and optimization of microstrip antenna arrays and their applications. He was PI of two projects funded from different funding agencies. He has participated in 13 research projects at the national and international levels under the Egypt–NSF–USA joint funds program, the, NTRA, STDF, National Authority of Remote Sensing, and so on.

ESMAT A. ABDALLAH (Member, IEEE) received the B.Sc., M.Sc., and Ph.D. degrees from the Faculty of Engineering, Cairo University, Giza, Egypt, in 1968, 1972, and 1975, respectively. She was nominated as an Assistant Professor, an Associate Professor, and a Professor, in 1975, 1980, and 1985, respectively. In 1989, she was appointed as the President of the Electronics Research Institute (ERI), Cairo, Egypt, a position she held for about ten years. She was the Head of the Microstrip Department, ERI, from 1999 to 2006. She is currently with the Microstrip Department, ERI. She has focused her research on microwave circuit designs, planar antenna systems, and nonreciprocal ferrite devices, and recently on EBG structures, UWB components and antenna and RFID systems. She acts as a single author and as a coauthor on more than 260 research articles in highly cited international journals and in proceedings of international conferences in her field. She supervised more than 80 M.Sc. and Ph.D. thesis. She was PI of more than 30 projects funded from different funding agencies. She has participated in many research projects at the national and international levels under the Egypt–NSF–USA joint funds program, the European Committee Programs FP7 program, NTRA, STDF, ITEDA, and so on. She is also a reviewer for many international societies. She was the authors of published books and chapter in Books in her field of interest. She also participated in many patents.

HADIA S. EL-HENNAWY (Member, IEEE) received the B.Sc. and M.Sc. degrees from Ain Shams University, Cairo, Egypt, in 1972 and 1976, respectively, and the Ph.D. degree from Technische Universitat Braunschweig, Germany, in 1982. In 1982, she returned to Egypt and joined the Electronics and Communications Engineering Department, Ain Shams University, as an Assistant Professor. She was nominated as an Associate Professor, in 1987, and then a Professor, in 1992. In 2004, she was appointed as the Vice-Dean for graduate study and research. In 2005, she was appointed as the Dean of the Faculty of Engineering, Ain Shams University. She has been the Head of the Microwave Research Laboratory, Ain Shams University, since 1982. She has published more than 100 journal and conference papers, and supervised more than 50 Ph.D. and M.Sc. students. She has focused her research on microwave circuit design, antennas, microwave communication, and recently wireless communication. She is a member of the Industrial Communication Committee in the National Telecommunication Regulatory Authority (NTRA), Educational Engineering Committee in the Ministry of Higher Education, and Space Technology Committee in the Academy of Scientific Research. She was the Editor in-Chief of the Faculty of Engineering, Ain Shams University, Scientific Bulletin, from 2004 to 2005. She is deeply involved in the Egyptian branch activities.

• • •